RF inhomogeneities correction in MRI T_1-weighted spin-echo image handling the non-multiplicative character of the bias field

Guylaine Collewet[a,b], Jérôme Idier[b]

[a] *Cemagref*
17, av de Cucillé, CS 64427, 35044, Rennes, France
phone: + (33)223482167, fax: + (33)223482115, email: guylaine.collewet@cemagref.fr
[b] *IRCCyN*
1 rue de la Noë, BP 92101, 44321 Nantes Cedex 3, France
phone: + (33)240376909, fax: + (33)240376930, email: Jerome.Idier@irccyn.ec-nantes.fr

Abstract

We propose a method to reduce the noise and to eliminate the effects of the inhomogeneity of the Radio-Frequency (RF) pulses and of the sensivity of the RF reception, particularly in the case of MR T_1-weighted images acquired with a low-field MRI system. In T_1-weighted images the effects of the pulse inhomogeneities vary with the tissues. Consequently the bias field is not strictly multiplicative and depends on the content of the image. In our approach, the MR signal is modeled as a sum of contributions of all the tissues present in the object. For the sake of generality, each pixel is assumed to contain an unknown proportion of each tissue, which thereby enables the method to cope with partial volume effect. The number of tissues composing the object as well as the MR characteristics of each tissue are assumed known. Several images with different acquisition parameter values are also needed. A penalized least-square criterion is proposed to estimate the RF emitted field, the RF sensitivity reception and the proportion of each tissue. The criterion incorporates smoothness regularization terms for both RF fields and for the proportion of each tissue in a view to reduce noise. We solve the optimization problem using a conjugate gradient algorithm within a block coordinate descent iterative scheme. Results based on simulation and on real MR images of fish acquired on a 0.2 T MRI demonstrate the effectiveness of the method.

Key words: MRI, noise, correction, inhomogeneity, T_1-weighted

1. Introduction

Magnetic resonance imaging (MRI) is an advanced technique providing valuable information in various application domains. In clinical applications, the sensitivity of MRI to tissue differentiation makes it the procedure of choice for detecting abnormalities or lesions in most parts of the body. However, the applications in industry are widespread. For example, the nuclear magnetic resonance (NMR) technique is sufficiently flexible to be used to measure the water/fat ratio in foods (Hills, 1998) or to study fluids in porous materials (Blümich, 2000). MRI can be used for visual inspection, as it is usually done in clinical examinations. In addition, quantitative information can be measured in the images. The quantitative information can be extracted using image segmentation or measurements directly based on the signal intensity. However, the process of magnetic resonance (MR) image formation introduces various artefacts that may corrupt a truly quantitative evaluation. A correction algorithm is then needed to overcome this problem.

The targeted application of our correction method

is the quantification of the anatomic distribution of fat tissues in fish. Because of the links between location of fat stores and product quality, precise data on distribution in different body compartments and within muscles are needed (Robb et al., 2002). MRI is a convenient technique to acquire these data. It easily provides 3D information and allows to differentiate between lipids and muscle using $\boldsymbol{T_1}$-weighted images. In this study, low-field MRI was used for the images acquisition. Low-field MRI (*i.e.,* using magnetic field values lower than 0.5 T) is not widely used in clinical applications. However, even though the signal-to-noise ratio (SNR) is lower than for high-field MRI, low-field MRI is able to achieve a diagnostic accuracy comparable to high-field scanners in many clinical cases (Merl et al., 1999). Besides its cost-effectiveness, low-field MRI can be "open designed" thus improving the patient comfort and allowing the access for interventional purpose (Daanen et al., 2000; Sequeiros et al., 2007). Moreover, artefacts linked to the strength of the field are less important at low-field than at high-field.

To further examine the question of artefacts, let us briefly recall the process of MR image formation: the MR signal is the sum of the radio-frequency (RF) signals issued from all the protons positionned in the permanent magnetic field B_0, and experimenting a sequence of pulses of RF magnetic field. This signal is acquired through a coil. A linear gradient of magnetic field $G(r)$ that depends on the position r is added to B_0. According to the Larmor law, the resulting signal frequency f_0 of the protons located on position r is proportional to $B_0 + G(r)$, so that the spatial density of the protons can be recovered by Fourier transform of the MR signal (Haacke et al., 1999).

RF inhomogeneities induce unwanted intensity variations of the signal, and their correction is the major issue addressed within this paper. On the other hand, all sources of uncontrolled modification of $B_0+G(r)$ may induce mislocalization errors. This is the case for the susceptibility difference between tissues, or between tissues and air, which induce local B_0 variations, the gradient non-linearity and the intrinsic inhomogeneity of B_0. Moreover, the chemical-shift of fat protons induces a difference between the signal frequency of fat and water protons, even if they are actually located at the same position. Contrary to the high-field case, all these phenomenons can be neglected at low-field provided the images are acquired in the zone where B_0 is homogeneous. Since we worked with a low-field MRI, we only considered RF inhomogeneities.

RF inhomogeneities are induced by two main sources:

- The sensitivity of the RF reception (RFR) coil is not homogeneous.
- Spatial inhomogeneities of the RF emission coil, coupled with off-resonance phenomenon linked to B_0 inhomogeneities, produce spatial variations of applied RF pulses (RFP), which in turn influence the signal intensity (Sled and Pike, 2000).

The inhomogenities due to RFP and RFR influence the image formation process in two different ways. The RFR effect can be considered as a multiplicative bias, while the influence of RFP depends on the proton longitudinal relaxation times T_1, particularly in spin-echo $\boldsymbol{T_1}$-weighted images (Wang et al., 2005). $\boldsymbol{T_1}$-weighted images are widely used in MR applications. The reason is twofold. Firstly, the contrast between tissues with different T_1 (such as fat and muscle, or gray matter, white matter and cerebrospinal fluid) is enhanced in such images. Secondly, because the acquisition time of $\boldsymbol{T_1}$-weighted images is reduced, due to the use of low values of TR.

Different approaches to the global problem of RF inhomogeneities can be found in the literature. Reviews can be found in Belaroussi et al. (2006); Hou (2006); Vovk et al. (2007). Some of them try to remove low-frequency variations of the signal. This is done with homomorphic filtering in Koivula et al. (1997); Brinkmann et al. (1998) or with a more sophisticated method where the bias field and the intensity distribution of true tissues are iteratively estimated (Sled et al., 1998). These approaches are not suited to applications where low-frequency variations of the signal are due to actual variations in the object. In order to incorporate a priori information, many authors proposed methods for the estimation of the bias field based on tissue segmentation. The expectation-maximization algorithm (EM) is used in Wells et al. (1996) to alternately estimate the bias and the statistical characteristics of each tissue. This algorithm was improved in Guillemaud and Brady (1997) thanks to the modeling of partial volume. EM was also chosen in Prima et al. (2001), where additional morphological information was taken from an atlas. Finally, some authors consider a Markov Random field model to describe spatial correlations (Zhang et al., 2001; Van Leemput et al., 1999). All such methods make the assumption that each pixel contains only one kind of tissue. While this is well-suited to the important case of cerebral imaging,

it does not correspond to the general situation, as found for example in MRI muscle examination (Marden et al., 2005), or in food products analysis such as fish (Toussaint et al., 2005) or bread (Grenier et al., 2003).

Finally, some authors proposed to use additional images in their correction scheme. In Condon et al. (1987); Tofts et al. (1994); McVeigh et al. (1986); Tincher et al. (1993) images of phantoms were used and considered as exact images of the bias field. An interesting hybrid approach is proposed in Fan et al. (2003) in the particular case of surface coils. An additional body coil image is used. It is supposed homogeneous but with low signal intensity. These methods do not make any assumptions on the objects. However, akin to the methods previously cited, they model the bias on the intensity using a smoothly varying, multiplicative field. As a consequence, they neglect the dependence between the T_1 of the tissues and the RFP inhomogeneities.

In this paper, we introduce a method that makes no assumption on the morphology of the imaged object. Moreover the particular effect of the RFP inhomogeneities linked to the T_1 is taken into account. As a price to pay for generality, several images under varied acquisition conditions are needed, either measured on the object of interest, or on a phantom composed of the relevant tissues. Moreover the tissues composing the object are supposed to be known. The signal of a voxel is modeled as the tissues contributions. Partial volume effect, that is the mixture of several tissues inside a voxel, is thus taken into consideration. The method estimates the tissue proportions, the RFR and the RFP inhomogeneity maps. It is based on the minimization of a regularized criterion. This criterion contains terms that account for data fidelity to the model and regularization terms which ensure smooth solution for RFR and RFP maps and for the tissue proportion map. A special regularization scheme is used for the tissue proportion maps in order to allow large intensity variations at the boundaries between regions. The use of the regularization terms allow to reduce the noise and thus to both correct and denoise the images in a unified approach. As our approach is based on the estimation of the tissue proportion in each voxel, it can be considered as a signal decomposition tool. It provides new quantities of interest which are the tissue proportions. Even though the initial objective was to estimate images free from artefacts, the tissue proportion map can also be considered as a result of the method.

The paper is organized as follows. In Section 2, the mathematical model behind our method is described. The signal model is first presented in the case of a unique tissue. Then, it is extended to the general case of partial volume voxels, and a penalized least square approach is proposed to estimate the unknown quantities. In Section 3 the solution of the resulting optimization problem is detailed. Section 4 details the conditions of simulation and of experimentation and section 5 is dedicated to results. First we present simulation results and finally results obtained on real images of a fish, acquired on a low-field imager. They demonstrate the efficiency of the method to quantify the proportion of fat and muscle with a view to a food product application. Finally some perspectives are proposed in Section 6.

2. Problem formulation

2.1. *Signal model*

2.1.1. *Case of a one-tissue homogeneous object*

In the simplified case of an homogeneous object containing only one tissue and under hypotheses detailed in Collewet et al. (2002), noting L the number of pixels, the noise-free spin-echo intensity s_ℓ at pixel $\ell = 1, \ldots, L$ can be modeled by:

$$s_\ell = R_\ell \, O f(\eta_\ell, \theta, T_1)$$

with $\theta = (\alpha, \beta, TR)$,

$$f(\eta_\ell, \theta, T_1) = \frac{1 - E_1}{2} \frac{\sin \eta_\ell \alpha \, (1 - \cos \eta_\ell \beta)}{1 - E_1 \cos \eta_\ell \alpha \, \cos \eta_\ell \beta}, \quad (1)$$

where $E_1 = \exp(-TR/T_1)$. $\boldsymbol{R} = (R_\ell)$ represents the reception coil sensitivity, $\boldsymbol{\eta} = (\eta_\ell)$ the attenuation factor for the nominal pulse angle, α the flip angle, β the angle of the refocusing pulse, O the *constant reference*, such that the signal for $(\boldsymbol{R}, \boldsymbol{\eta}, \alpha, \beta) = (\mathbf{1}, \mathbf{1}, 90°, 180°)$ is equal to $O(1 - E_1)$, and T_1 the longitudinal relaxation time of the tissue.

$\boldsymbol{R}$ and $\boldsymbol{\eta}$ respectively represent the sensitivity of the reception coil, RFR, and the spatial inhomogeneity of the RF pulses, RFP. In what follows, all 2D arrays indexed by ℓ, such as $\boldsymbol{\eta}$ and $\boldsymbol{R}$, will rather be treated as $L \times 1$ vectors.

Would the signal s_ℓ be free from any inhomogeneity, it would read:

$$s^*_\ell = O f(1, \theta, T_1).$$

Therefore, the actual noise-free version s_ℓ takes the following form:

$$s_\ell = s^*_\ell R_\ell \frac{f(\eta_\ell, \theta, T_1)}{f(1, \theta, T_1)} = s^*_\ell M_\ell N_\ell,$$

where

$$M_\ell = R_\ell \frac{\sin \eta_\ell \alpha \, (1 - \cos \eta_\ell \beta)}{\sin \alpha \, (1 - \cos \beta)} \tag{2}$$

is a purely multiplicative bias component since it does not depend on the imaged tissue, while

$$N_\ell = \frac{1 - E_1 \cos \alpha \cos \beta}{1 - E_1 \cos \eta_\ell \alpha \, \cos \eta_\ell \beta} \tag{3}$$

is a non-multiplicative bias since its value depends on T_1 through E_1, and consequently on the tissue itself.

Actually, there is also a dependence of $\boldsymbol{R}$ and $\boldsymbol{\eta}$ on the geometry and composition of the imaged object. However, in the case of low-field MR systems, such a dependence is rather weak (Sled and Pike, 1998). For the sake of tractable analysis, it will not be taken into account here.

Figure 1 shows the values of the non-multiplicative bias term N_ℓ as a function of η_ℓ and the ratio TR/T_1, in the case of $\boldsymbol{T_1}$-weighted images with $TR/T_1 < 1.5$, for $\alpha = 90°$ and $\beta = 180°$. A preliminary study showed that the range for η in a 0.2−T MR system equipped with a head coil was between 0.85 and 1.15. This is due both to RFP inhomogeneity and to systematic reduction of the flip angle decided by the constructor to reduce the energy received by the patient. For values of η around 1, the bias field is equal to 1 and corresponds to no signal inhomogeneity induced by the RFP inhomogenities. For values of η greater than 1, the bias increases up to 1.15 for low values of TR/T_1. For values of η lower than 1 the bias decreases down to 0.9 and is the lowest for low values of TR/T_1. In the presence of several tissues with different values of TR/T_1, as envisaged in the following, this clearly corresponds to a non-multiplicative behavior since the different tissues will yield signal components with different functions $N_{\ell i}$, without proportionality relation between them. For instance, TR/T_1 is equal to 1.4 for fat and 0.28 for muscle, for $TR = 140$ at $0.2T$.

Depending on the accuracy required, it may be necessary to correct the images from this non-multiplicative bias. However, this bias depends on the T_1 of the tissue inside each voxel. Moreover, several tissues (two in most cases), with different T_1 values, may be present in the voxels. So, in order to cope with realistic situations, the model of the signal must be extended to the case of objects that are made of several components (or tissues).

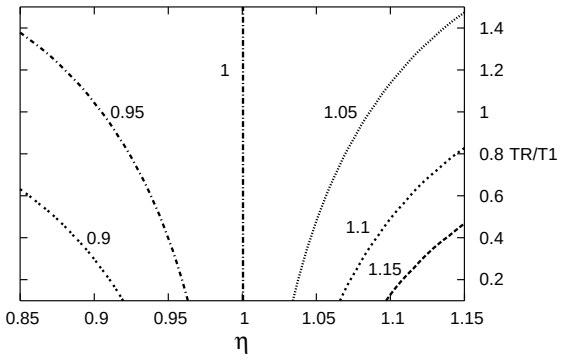

Fig. 1. Value of the non-multiplicative bias term (3) as a function of η_ℓ and TR/T_1 for $\alpha = 90°$ and $\beta = 180°$.

2.1.2. *General case of an object composed of several tissues*

Let us consider an object composed of I tissues (*e.g.,* fat, muscle, grey and white matter, ...), in the case of a spin-echo sequence where the additivity of the signals is valid. Then, for each pixel ℓ, the signal can be modeled by:

$$s_\ell = R_\ell \sum_{i=1}^{I} k_{\ell i} O_i f(\eta_\ell, \theta, T_{1i}) + n_\ell$$

where f is still defined by (1), $k_{\ell i} \in [0, 1]$ is the proportion of tissue i in pixel ℓ, O_i the constant reference of tissue i, T_{1i} the longitudinal relaxation time of tissue i and $\boldsymbol{n} = (n_\ell)$ the noise component. $\theta = (\alpha, \beta, TR)$ can be considered as a vector of known parameters chosen by the MR operator. Finally, if the pixels are all assumed to be fully filled with tissues, *i.e.,* the case of pixels partially containing air is excluded, the following relation is verified:

$$\sum_{i=1}^{I} k_{\ell i} = 1, \qquad \forall \ell = 1, \ldots, L. \tag{4}$$

Our goal is to retrieve the signal s^* that would be issued from a perfect MR system, that is, for $(\boldsymbol{R}, \boldsymbol{\eta}, \boldsymbol{n}) = (\mathbf{1}, \mathbf{1}, \mathbf{0})$:

$$s^*_\ell = \sum_{i=1}^{I} k_{\ell i} O_i f(1, \theta, T_{1i}).$$

Since $\boldsymbol{R}$ and $\boldsymbol{O} = (O_i)$ are linked multiplicatively, all couples $(C\boldsymbol{R}, \boldsymbol{O}/C)$ (with $C > 0$) are equivalent from the measurement viewpoint. To raise this undeterminacy, we propose to assume that the quantities O_i are known, since they can be measured during a calibration step. For example, the intensity of

regions containing only one tissue can be measured manually once for all with pixels filled with tissue i in the center of the system where $\boldsymbol{R}$ and η can be assumed equal to 1. We also rely on a sufficiently good knowledge of T_{1i}, since relaxation times can be precisely measured using NMR experiments. Thus the remaining unknown variables are $\boldsymbol{R}$, $\boldsymbol{\eta}$ and $\boldsymbol{k} = (k_{\ell i})$, which amounts to $I+2$ images, *i.e.,* $(I+1)\times N$ scalar unknowns given constraint (4). In order to build reliable estimates, we propose to acquire $J \geq I+1$ images $\boldsymbol{s}_j = (s_{j\ell})$, using different values for the triple θ. Such a procedure necessarily increases the acquisition time compared to the acquisition of a single image. There are several ways of circumventing this problem. On the one hand, images of phantoms acquired once for all can be used as one part of the J images. On the other hand, it is possible to decrease the number of signal averagings. Signal averaging is typically used in MRI to increase the SNR. As shown later in the article, the regularization scheme reduces the noise effect and thus it may allow the use of images at a lower SNR, acquired in a shorter time.

2.2. *Cost function definition*

$\boldsymbol{R}$ and $\boldsymbol{\eta}$ depend on the antennae configuration but can be considered smooth, since they are governed by the Biot-Savart law. The magnetic field created by an antennae does not exhibit high frequency spatial variations. In a view to reduce the noise, some regularization on the tissue proportions $\boldsymbol{k}$ can also be introduced. However, it should be carefully designed, so that large variations of the signal be not penalized at the boundaries between distinct regions of the object. In the sequel, we adopt an approach so-called *edge-preserving* in the field of image restoration.

Thus we propose to estimate $\boldsymbol{R}$, $\boldsymbol{k}$ and $\boldsymbol{\eta}$ using a penalized least-square approach:

$$(\hat{\boldsymbol{R}}, \hat{\boldsymbol{k}}, \hat{\boldsymbol{\eta}}) = \arg\min_{\boldsymbol{R},\boldsymbol{k},\boldsymbol{\eta}} \mathcal{J}(\boldsymbol{R}, \boldsymbol{k}, \boldsymbol{\eta}) \quad \text{subject to (4)},$$

where

$$\mathcal{J}(\boldsymbol{R}, \boldsymbol{k}, \eta) = \sum_{j=1}^{J} \lambda_j \sum_{\ell=1}^{L} \left(s_{j\ell} - R_\ell \sum_{i=1}^{I} O_{ji} k_{\ell i} f_{ij\ell} \right)^2 + \gamma_R \left\| \mathbf{D}\boldsymbol{R} \right\|^2 + \gamma_\eta \left\| \mathbf{D}\boldsymbol{\eta} \right\|^2 + \gamma_k \sum_{c \in \mathcal{C}} \phi\big(\|\boldsymbol{d}_c^{\mathrm{t}} \boldsymbol{k}\| \big). \quad (5)$$

with $f_{ij\ell} = f(\eta_\ell, \theta_j, T_{1i})$, $\phi(u) = \sqrt{\delta^2 + u^2}$, and $\|\cdot\|$ denotes the usual L_2 norm. O_{ji} corresponds to the constant reference of tissue i for signal j. Parameters λ_j, γ_R, γ_η and γ_k are positive weights, and δ is a scalar. $\mathcal{C}$ represents the set of the pairs of adjacent pixels $c = \{r, s\}$, with $r < s$ for an arbitrary ordering. $\boldsymbol{d}_c$ is the $L \times 1$ finite difference vector such that $\boldsymbol{d}_c^{\mathrm{t}} \boldsymbol{k} = [k_{r_1} - k_{s_1}, \cdots, k_{r_I} - k_{s_I}]^{\mathrm{t}}$. Finally, $\mathbf{D} = [d_1, \cdots, d_C]^{\mathrm{t}}$ is a $C \times L$ matrix, where $C = \#\mathcal{C}$.

The first term in (5) accounts for data fidelity, the second and third terms respectively ensure a smooth solution for $\boldsymbol{R}$ and $\boldsymbol{\eta}$ and the fourth term tends to decrease the noise in $\boldsymbol{k}$ while allowing rapid variations. Indeed, function ϕ has a quadratic behavior near 0 and an asymptotically linear behavior (see Figure 2). For large values of $\|\boldsymbol{d}_c^{\mathrm{t}} \boldsymbol{k}\|$, that is for large values of differences between the vector proportion of adjacent pixels, the regularizing term will be lower than it would have been using a quadratic regularization. This allows to penalize variations of $\boldsymbol{k}$ depending on the value of these variations.

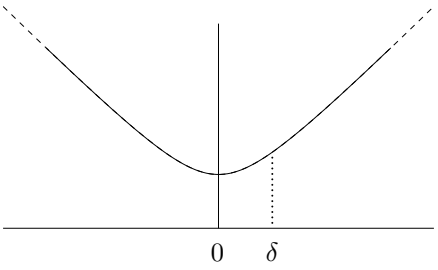

Fig. 2. Variations of $\phi(u) = \sqrt{\delta^2 + u^2}$, $\delta > 0$.

3. Solution to the optimization problem

3.1. *Block coordinate descent*

We propose to resort to a block coordinate descent (BCD) approach to compute $\hat{\boldsymbol{R}}$, $\hat{\boldsymbol{\eta}}$ and $\hat{\boldsymbol{k}}$. BCD algorithms are guarantied to converge towards a local minimizer of the criterion, under large mathematical conditions (Bezdek et al., 1987).

(i) While $\boldsymbol{\eta}$ and $\boldsymbol{k}$ are held at their current value, a fixed number of iterations of a conjugate gradient (CG) algorithm are performed to minimize $\mathcal{J}$ with respect to (w.r.t.) $\boldsymbol{R}$.

(ii) While $\boldsymbol{R}$ and $\boldsymbol{k}$ are held at their current value, a fixed number of iterations of a CG algorithm are performed to minimize $\mathcal{J}$ w.r.t. $\boldsymbol{\eta}$.

(iii) While $\boldsymbol{R}$ and $\boldsymbol{\eta}$ are held at their current value, a fixed number of iterations of a CG algorithm are performed to minimize $\mathcal{J}$ w.r.t. $\boldsymbol{k}$, subject to constraint (4).

Steps (i), (ii) and (iii) are performed repeatedly, until the norm of the gradient of $\mathcal{J}$ w.r.t. $(\boldsymbol{R}, \boldsymbol{\eta}, \boldsymbol{k})$ becomes sufficiently small, *i.e.,* $\|\nabla\mathcal{J}(\boldsymbol{R}, \boldsymbol{\eta}, \boldsymbol{k})\| \leq \varepsilon$.

3.2. *Minimization w.r.t.* $\boldsymbol{R}$ *(Step* (i)*)*

Let $\circ$ denote the Hadamard (*i.e.,* entrywise) matrix product, and $\boldsymbol{\delta}_j$ the $L \times 1$ vector with entries $\sum_i O_{ji} k_{\ell i} f_{ij\ell}$, for $\ell = 1, \ldots, L$. Then, it is straightforward to express the gradient component $\nabla_{\boldsymbol{R}}\mathcal{J}$ under the following form :

$$\nabla_{\boldsymbol{R}}\mathcal{J}(\boldsymbol{R}, \boldsymbol{k}, \eta) = 2\sum_{j=1}^{J} \lambda_j \, \boldsymbol{\delta}_j \circ (\boldsymbol{\delta}_j \circ \boldsymbol{R} - \boldsymbol{s}_j) + 2\gamma_R \mathbf{D}^{\mathrm{t}}\mathbf{D}\boldsymbol{R}, \quad (6)$$

with $\boldsymbol{s}_j = (s_{jl})$. Equation $\nabla_{\boldsymbol{R}}\mathcal{J}(\boldsymbol{R}, \boldsymbol{k}, \eta) = 0$ amounts to solving a $L \times L$ linear system. It is actually more efficient to adopt a CG approach, and even an overrelaxed version of CG, in a view to accelerate the convergence of the algorithm. The update equation then takes the following form

$$\boldsymbol{R}^{(n)} = \omega\hat{\boldsymbol{R}}^{(n)} + (1-\omega)\boldsymbol{R}^{(n-1)},$$

where n is the iteration number, $\hat{\boldsymbol{R}}^{(n)}$ (respectively, $\boldsymbol{R}^{(n)}$) is the result of the non-relaxed version of CG after a given small number of iterations, and ω is the relaxation parameter. Convergence is ensured if $\omega\,(0, 2)$, and it is faster if $\omega \in (1, 2)$ (Press et al., 1988). We empirically set $\omega = 1.8$.

3.3. *Minimization w.r.t.* $\boldsymbol{\eta}$ *(Step* (ii)*)*

$\mathcal{J}$ is a complex, possibly multimodal function of $\boldsymbol{\eta}$. Therefore, the minimization result may be sensible to the initial point. The components of $\boldsymbol{\eta}$ are expected to vary between 0.6 and 1.3, so it is reasonable to choose $\boldsymbol{\eta} = \mathbf{1}$ as initial point. The CG algorithm is then used to determine a search direction. The gradient component $\nabla_{\boldsymbol{\eta}}\mathcal{J}$ takes the following form:

$$\nabla_{\boldsymbol{\eta}}\mathcal{J}(\boldsymbol{R}, \boldsymbol{k}, \eta) = 2\boldsymbol{R} \circ \sum_{j=1}^{J} \lambda_j \, \boldsymbol{\delta}'_j \circ (\boldsymbol{\delta}_j \circ \boldsymbol{R} - \boldsymbol{s}_j) + 2\gamma_\eta \mathbf{D}^{\mathrm{t}}\mathbf{D}\boldsymbol{\eta}, \quad (7)$$

where $\boldsymbol{\delta}'_j$ is a $L \times 1$ vector with entries $\sum_i O_{ji} k_{\ell i} f'_{ij\ell}$, and $f'_{ij\ell} = \partial f_{ij\ell}/\partial\eta_\ell$. The explicit expression of the latter term is omitted here, since it is lengthy but easy to establish.

On the other hand, we have been unable to determine a closed form for the optimal stepsize in the prescribed direction. Therefore, a suboptimal stepsize strategy has been rather adopted, based on the fact that the Hessian of $\mathcal{J}$ w.r.t. $\boldsymbol{\eta}$ is upper bounded, as shown in Appendix. According to Böhning and Lindsay (1988) and Lange et al. (2000), such a condition ensures that $\mathcal{J}$ admits an upper quadratic approximation. Therefore, Assumption A.3 of Labat and Idier (2007) is fulfilled, so that the local convergence of the resulting CG algorithm is granted, according to (Labat and Idier, 2007, Theorem 4.1).

3.4. *Minimization w.r.t.* $\boldsymbol{k}$ *(Step* (iii)*)*

Step (iii) corresponds to the minimization of $\mathcal{J}$ as a function of $\boldsymbol{k}$. Since ϕ is strictly convex, it can be easily shown that $\mathcal{J}$ is strictly convex w.r.t. $\boldsymbol{k}$, and therefore, a unimodal function of $\boldsymbol{k}$. Again, we used a limited number of CG iterations with the suboptimal stepsize strategy proposed in Labat and Idier (2007).

The following expression of the gradient component $\nabla_{\boldsymbol{k}}\mathcal{J}$ (displayed as a $L \times I$ matrix) can be derived:

$$\nabla_{\boldsymbol{k}}\mathcal{J}(\boldsymbol{R}, \boldsymbol{k}, \eta) = 2\sum_{j=1}^{J} \lambda_j \mathbf{V}_j \circ \left((\boldsymbol{\delta}_j \circ \boldsymbol{R} - \boldsymbol{s}_j)\,\mathbf{1}_I^{\mathrm{t}}\right) + 2\gamma_k \sum_{c\in\mathcal{C}} \frac{\phi'\left(\|\boldsymbol{d}_c^{\mathrm{t}}\boldsymbol{k}\|\right)}{\|\boldsymbol{d}_c^{\mathrm{t}}\boldsymbol{k}\|} \boldsymbol{d}_c\boldsymbol{d}_c^{\mathrm{t}}\boldsymbol{k}. \quad (8)$$

where $\mathbf{1}_I$ is the $I \times 1$ unit vector, and $\mathbf{V}_j$ is a $L \times I$ matrix with entries $O_{ji} R_\ell f_{ij\ell}$.

To take constraint (4) into account, a simple and efficient solution is to replace the gradient $\nabla_{\boldsymbol{k}}\mathcal{J}$ by its projection onto the hyperplane defined by (4) (Luenberger, 1997), *i.e.,*

$$\boldsymbol{g}_k = \nabla_{\boldsymbol{k}}\mathcal{J} - \nabla_{\boldsymbol{k}}\mathcal{J}\mathbf{1}_I\mathbf{1}_I^{\mathrm{t}}/I.$$

The resulting CG scheme is ensured to converge to the unique minimizer of $\mathcal{J}$ as a function of $\boldsymbol{k}$, under constraint (4).

See Table 1 for the detailed algorithm.

$\boldsymbol{R} \leftarrow \mathbf{1}_L$ % Initialization
$\boldsymbol{\eta} \leftarrow \mathbf{1}_L$ %
$\boldsymbol{k} \leftarrow \mathbf{1}_L \mathbf{1}_I^{\mathrm{t}}/I$ %

repeat % Main loop
 %----------
 % Step (i): linear CG w.r.t. $\boldsymbol{R}$
 %----------
 $\boldsymbol{g}_R \leftarrow \nabla_{\boldsymbol{R}} \mathcal{J}$ % $\nabla_{\boldsymbol{R}} \mathcal{J}$ is given by (6)
 for $n_R = 1 : N_R$ **do**
  $\rho_R = \|\boldsymbol{g}_R\|^2$
  if $n_R = 1$ **then**
   $\boldsymbol{p}_R \leftarrow -\boldsymbol{g}_R$
  else
   $\boldsymbol{p}_R \leftarrow -\boldsymbol{g}_R + (\rho_R/\rho_R^{\mathrm{old}})\boldsymbol{p}_R$
  end if
  $\boldsymbol{w}_R \leftarrow 2\sum_j \lambda_j \boldsymbol{\delta}_j \circ \boldsymbol{\delta}_j \circ \boldsymbol{p}_R + 2\gamma_R \mathbf{D}^{\mathrm{t}}\mathbf{D}\boldsymbol{p}_R$
  $\mu_R \leftarrow \rho_R/\boldsymbol{p}_R^{\mathrm{t}}\boldsymbol{w}_R$
  $\boldsymbol{R} \leftarrow \boldsymbol{R} + \mu_R \boldsymbol{p}_R$
  $\boldsymbol{g}_R \leftarrow \boldsymbol{g}_R + \mu_R \boldsymbol{w}_R$
  $\rho_R^{\mathrm{old}} \leftarrow \rho_R$
 end for
 $\boldsymbol{R}^{\mathrm{old}} \leftarrow \boldsymbol{R} \leftarrow \omega \boldsymbol{R} + (1-\omega)\boldsymbol{R}^{\mathrm{old}}$
 %----------
 % Step (ii): Polak-Ribiere nonlinear CG w.r.t. $\boldsymbol{\eta}$
 %----------
 for $n_\eta = 1 : N_\eta$ **do**
  $\boldsymbol{g}_\eta \leftarrow \nabla_{\boldsymbol{\eta}} \mathcal{J}$; % $\nabla_{\boldsymbol{\eta}} \mathcal{J}$ is given by (7)
  if $n_\eta = 1$ **then**
   $\boldsymbol{p}_\eta \leftarrow -\boldsymbol{g}_\eta$
  else
   $\beta_\eta \leftarrow (\boldsymbol{g}_\eta - \boldsymbol{g}_\eta^{\mathrm{old}})^{\mathrm{t}}\boldsymbol{g}_\eta / \|\boldsymbol{g}_\eta^{\mathrm{old}}\|^2$
   $\boldsymbol{p}_\eta \leftarrow -\boldsymbol{g}_\eta + \beta_\eta \boldsymbol{p}_\eta$
  end if
  $\mu_\eta \leftarrow -\boldsymbol{p}_\eta^{\mathrm{t}}\boldsymbol{g}_\eta / \boldsymbol{p}_\eta^{\mathrm{t}}\mathbf{M}\boldsymbol{p}_\eta$ % $\mathbf{M}$ is sparse and
  $\boldsymbol{\eta} \leftarrow \boldsymbol{\eta} + \mu_\eta \boldsymbol{p}_\eta$ % computable once
  $\boldsymbol{g}_\eta^{\mathrm{old}} \leftarrow \boldsymbol{g}_\eta$ % for all using (15)
 end for
 %----------
 % Step (iii): Polak-Ribiere nonlinear CG w.r.t. $\boldsymbol{k}$
 %----------
 % Here, for all matrix $\mathbf{M}$, $\overrightarrow{\mathbf{M}}$ stands for a column
 % vector with elements taken columnwise from $\mathbf{M}$
 for $i = 1 : N_k$ **do**
  $\boldsymbol{g}_k \leftarrow \nabla_{\boldsymbol{k}} \mathcal{J} - \nabla_{\boldsymbol{k}} \mathcal{J} \mathbf{1}_I \mathbf{1}_I^{\mathrm{t}}/I$ % $\nabla_{\boldsymbol{k}} \mathcal{J}$ is given by (8)
  if $n_k = 1$ **then**
   $\boldsymbol{p}_k \leftarrow -\boldsymbol{g}_k$
  else
   $\beta_k \leftarrow (\overrightarrow{\boldsymbol{g}_k} - \overrightarrow{\boldsymbol{g}_k}^{\mathrm{old}})^{\mathrm{t}}\overrightarrow{\boldsymbol{g}_k} / \|\overrightarrow{\boldsymbol{g}_k}^{\mathrm{old}}\|^2$
   $\boldsymbol{p}_k \leftarrow -\boldsymbol{g}_k + \beta_k \boldsymbol{p}_k$
  end if
  $\forall c, q_c \leftarrow \phi'(\|\boldsymbol{d}_c^{\mathrm{t}}\boldsymbol{k}\|)/\|\boldsymbol{d}_c^{\mathrm{t}}\boldsymbol{k}\|$
  $D \leftarrow 2\sum_j \lambda_j \|\overrightarrow{\mathbf{V}_j \circ \boldsymbol{p}_k}\|^2 + \gamma_k \sum_c q_c \|\boldsymbol{d}_c^{\mathrm{t}}\boldsymbol{p}_k\|^2$
  $\mu_k \leftarrow -\overrightarrow{\boldsymbol{p}_k}^{\mathrm{t}}\overrightarrow{\boldsymbol{g}_k}/D$
  $\boldsymbol{k} \leftarrow \boldsymbol{k} + \mu_k \boldsymbol{p}_k$
  $\boldsymbol{g}_k^{\mathrm{old}} \leftarrow \boldsymbol{g}_k$
 end for
until $\|\nabla \mathcal{J}(\boldsymbol{R}, \boldsymbol{\eta}, \boldsymbol{k})\| \leq \varepsilon$ % End of main loop

Table 1
Block coordinate descent algorithm

4. Material: images and algorithm parameters

The proposed algorithm has been tested on both simulated and real images. The simulated and real acquisition conditions are presented first. Then the algorithm parameter values are given, and finally the estimation results are provided and commented.

4.1. *Acquisition conditions*

We chose to use images of fat fishes (such as salmon and trout) to evaluate the performance of our estimation method. Fish is made of two tissues, fat and muscle, with approximatively known T_1. From NMR measurements, it was evaluated that $T_1 \approx 110$ ms for fat and $T_1 \approx 500$ ms for muscle. In such a case of two tissues, the minimum number of images required is three.

- A single image $\boldsymbol{s}_1$ was acquired on the object of interest, and the corresponding acquisition parameters were $\theta_1 = (\alpha_1, \beta_1, TR_1) = (90°, 180°, 140 \text{ ms})$, which provides $\boldsymbol{T_1}$-weighted images with a high contrast between fat and muscle.
- Two other images $(\boldsymbol{s}_2, \boldsymbol{s}_3)$ were measured once for all on a cylinder filled with oil. The acquisition parameters were, respectively: $\theta_2 = (\alpha_2, \beta_2, TR_2) = (60°, 180°, 700 \text{ ms})$ and $\theta_3 = (\alpha_3, \beta_3, TR_3) = (120°, 180°, 700 \text{ ms})$.

4.2. *Definition of a mask to exclude background voxels*

In the acquired images, the background voxels do not fulfill constraint (4), since no tissue is present there. The corresponding data can be easily detected using a simple threshold test, and we propose to exclude them from the correction process. Mathematically, it simply amounts to reduce the size of the dataset and of the unknown maps $\boldsymbol{R}$, $\boldsymbol{k}$ and $\boldsymbol{\eta}$, and to redefine the set of difference vectors $(\boldsymbol{d}_c)$ accordingly. Then, the new criterion to be minimized takes an expression similar to (5). Therefore, this modification remains implicit in what follows.

4.3. *Algorithm parameters*

No prior information was assumed on the values of the maps $\boldsymbol{R}$, $\boldsymbol{\eta}$, $\boldsymbol{k}_1$ and $\boldsymbol{k}_2$. Each of them was

initialized as a constant image: $\boldsymbol{R}^{(0)} = \boldsymbol{\eta}^{(0)} = \mathbf{1}$, and $\boldsymbol{k}_1^{(0)} = \boldsymbol{k}_2^{(0)} = \mathbf{1}/2$. A fixed number of five iterations was adopted for each of the three CG loops.

One keypoint of our method is the choice of the hyperparameters λ_j,γ_R, γ_η, γ_k and δ. According to the probabilistic interpretation of criterion $\mathcal{J}$, λ_j corresponds to the inverse of the noise variance for the jth image. The noise variances can be estimated directly from the images using the method proposed in Nowak (1999). In order to choose the remaining parameters γ_R, γ_η, γ_k and δ we run successive simulations with γ_R and $\gamma_\eta \in \{0, 1e^1, 1e^2, 1e^3, 1e^4, 1e^5, 1e^6, 1e^7, 1e^8\}$, $\gamma_k \in \{0, 1, 1e^1, 1e^2, 1e^3\}$ and $\delta \in \{0.1, 0.2, 0.3, 0.4, 0.5, 0.6\}$. The sets of value for γ_R, γ_η and γ_k were chosen empirically since no probable value can be inferred *a priori*. On the contrary, the value for δ can be compared with the value of $\|\boldsymbol{d}_c\boldsymbol{k}\|$ which corresponds to the difference between the tissue proportion of one pixel and of the pixels of the corresponding clique $\mathcal{C}$. Indeed, δ can be considered as a threshold above which the ϕ function is no more quadratic. As $\boldsymbol{k}_i$ represents tissue proportion $\in \{0, 1\}$, we chose values from 0.1 to 0.6 for δ.

For the simulations, we stopped the coordinate descent when the evolution of the estimation error was smaller than a threshold. We defined the estimation error ϵ_k as the L_1 error norm between the actual values $\boldsymbol{k}^{\text{act}}$ and the estimated values $\boldsymbol{k}^{\text{est}}$ expressed in %:

$$\epsilon_k = 100 \sum_{\ell=1}^{L} \sum_{i=1}^{I} |k_{\ell i}^{\text{act}} - k_{\ell i}^{\text{est}}|.$$

We stopped when $|(\epsilon_k(n) - \epsilon_k(n-1))|$, with n the number of iterations, became lower than 10^{-2} and we limited the number of iterations to 1000.

For the results using real images, we stopped the coordinate descent when $\|\nabla\mathcal{J}(\boldsymbol{R}, \boldsymbol{\eta})\|$ became lower than $\varepsilon = 3L \times 10^{-2}$ and we limited the number of iterations to 1000.

4.4. *Comparative algorithm using a direct approach*

In order to evaluate the performance of this correction method, let us compare it with an existing method proposed in Collewet et al. (2002). The latter is restricted to particular values of the acquisition parameters, and it is based on the inversion of the observation equations under noise-free hypothesis. Using θ_2 and θ_3 previously described to acquire images on an homogeneous object with $T_1 \approx 100$ ms, we can consider that $E_1 \approx 0$ since $T_1 \ll TR$. Moreover, since $\alpha_3 = 2\alpha_2$ and $\beta_3 = \beta_2$, we obtain, up to the presence of noise:

$$\begin{cases} 1 = k_{\ell 1} + k_{\ell 2} \\ s_{1\ell} = R_\ell \sum_{i=1}^{2} k_{\ell i} O_i f_{i1\ell} \\ s_{2\ell} = R_\ell \, O_h \sin \eta_\ell \alpha_2 \, (1 - \cos \eta_\ell \beta_2) \\ s_{3\ell} = R_\ell \, O_h \sin 2\eta_\ell \alpha_2 \, (1 - \cos \eta_\ell \beta_2) \end{cases}$$

where O_h is the constant reference of the homogeneous product. With the prior knowledge of T_{11}, T_{12}, O_1, O_2 and O_h, we can easily deduce $k_{\ell 1}$, $k_{\ell 2}$, η_ℓ and R_ℓ from this system of equations:

$$\begin{cases} \eta_\ell = \dfrac{1}{\alpha_2} \arccos \dfrac{s_{3\ell}}{2 s_{2\ell}} \\ R_\ell = \dfrac{s_{2\ell}}{O_h \sin \eta_\ell \alpha_2 \, (1 - \cos \eta_\ell \beta_2)} \\ k_{\ell 1} = \dfrac{1}{R_\ell} \dfrac{s_{1\ell} - O_2 f_{21\ell}}{O_1 f_{11\ell} - O_2 f_{21\ell}} \\ k_{\ell 2} = 1 - k_{\ell 1} \end{cases} \tag{9}$$

This method is clearly of restricted application. However, it has the advantage to be very simple to implement and of very low computational cost. It will be subsequently referred to as the "direct method", in contrast with the inverse problem resolution approach proposed in this paper.

4.5. *Material for simulated images*

A virtual image $\boldsymbol{s}_1$ of a trout was built from a real fish, using the direct method applied to an MRI acquisition at a high SNR value. It is depicted on Figure 3. The highest gray levels correspond to fat tissues and the lowest to muscle. Due to the trout physiology and to the relative thickness of the slices, many pixels contain both fat and muscle. Let us remark here that such a configuration is definitively not suited to segmentation based approaches.

Two additional images $(\boldsymbol{s}_2, \boldsymbol{s}_3)$ were computed, simulating an image acquired on an homogeneous product. $\boldsymbol{R}$ and $\boldsymbol{\eta}$ were also taken from a real example. Gaussian noise was added to the three images. Noise in MR magnitude images is governed by a Rician distribution (Sijbers et al., 1998). However, for SNR values larger than 3 dB, which is the case in most applications, it can be considered as white Gaussian. The standard deviation of the added noise was respectively 100 for $\boldsymbol{s}_1$ and 30 for $\boldsymbol{s}_2$ and $\boldsymbol{s}_3$. Less noise was added to the latter two, since they

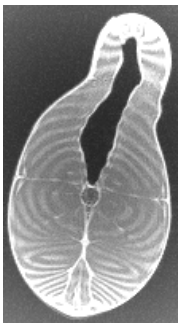

Fig. 3. $\boldsymbol{s}_1$ used for the simulations.

correspond to images acquired one for all, and thus they can be acquired with a longer acquisition time. This values are to be compared with the signal values. The mean signal values were respectively 650, 2000 and 2200 for $\boldsymbol{s}_1$, $\boldsymbol{s}_2$ and $\boldsymbol{s}_3$.

4.6. *Material for real images*

We also tested our algorithm on real images.

$\boldsymbol{s}_1$ was acquired on a trout, and $(\boldsymbol{s}_2, \boldsymbol{s}_3)$ on a cylinder filled with oil. The MRI system was a 0.2 T imager (Open, Siemens). The fish was kept refrigerated at 5°C to avoid signal variations due to temperature. Five different images $\boldsymbol{s}_1^1, \ldots, \boldsymbol{s}_1^5$ of the same slice of the fish were actually acquired after a translation of 22.5 mm between each acquisition, along the z axis (*i.e.,* perpendicularly to the slice plane).

Two levels of noise were obtained with two different numbers of signal averagings, in a view to explore the performance of the denoising capacity of our algorithm. No averaging was performed for one set of images, called hereafter "high-noise images", while a second set of so-called "low-loise images" was obtained after ten averagings.

The field of view was 200 mm × 200 mm and the matrix size was $N = 256 \times 256$. The slice thickness was 4 mm for $\boldsymbol{s}_1$ and 10 mm for $\boldsymbol{s}_2$ and $\boldsymbol{s}_3$. The latter value was used to increase the SNR. Since $\boldsymbol{s}_2$ and $\boldsymbol{s}_3$ were acquired on an homogeneous object, it was not at the expense of a lower resolution.

The quantities O_i were directly measured on $\boldsymbol{s}_1$: a region filled with fat was manually selected, and the corresponding mean intensity was computed. Similarly, a region physiologically known as very low-fat (less than 1%) was chosen to compute the muscle signal.

5. Results

5.1. *Simulation results*

5.1.1. *Influence of the hyperparameters*

We run the simulations for all the combinations of the parameters. The best results (*i.e.,* corresponding to the lowest value of ϵ_k) were found for

$$\gamma_R = 1e^5, \gamma_\eta = 1e^3, \gamma_k = 1e^1, \delta = 0.3. \qquad (10)$$

Figure 4 shows the evolution of the error for $\gamma_k = 1e^1$ and $\delta = 0.3$ in function of γ_R and γ_η. Note that the scales are in logarithm for γ_R, γ_η and γ_k. Figure 5 shows the evolution of ϵ_k for $\gamma_R = 1e^5$ and $\gamma_\eta = 1e^3$ in function of γ_k and δ.

Figure 4 shows a limited sensivity of the L_1 error norm ϵ_k w.r.t. γ_R and γ_η. The sensitivity w.r.t. γ_η is indeed very low: from the lowest to the highest value of γ_η, ϵ_k only varies from 4.5 to 7%. It is more sensible to γ_R, since too large values of γ_R produce quite large error values. Finally, the influence of the accuracy of estimation of $\boldsymbol{R}$ on the results is more important than the estimation of $\boldsymbol{\eta}$. This can be easily deduced from the expression of $k_{\ell 1}$ in function of R_ℓ and η_ℓ in system (9): the sensitivity of $k_{\ell 1}$ in function of R_ℓ is higher than in function of η_ℓ.

Figure 5 shows a relatively higher sensivity to the value of γ_k, although the choice of this parameter gives the same error when varying from 1 to 100. On the other hand, parameter δ seems to have a very limited influence on the result.

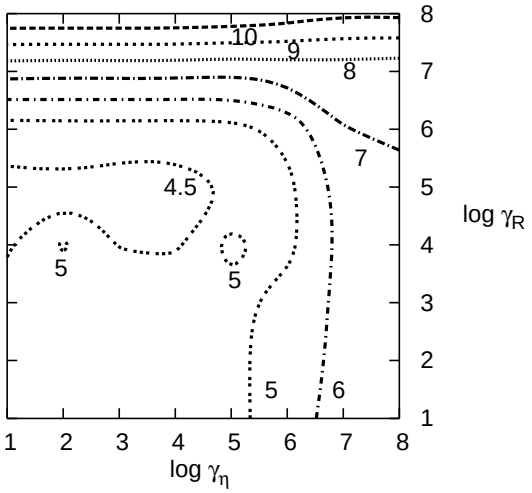

Fig. 4. Contour plot of L_1 error norm ϵ_k for $\gamma_k = 1e^1$ and $\delta = 0.3$ in function of γ_R and γ_η.

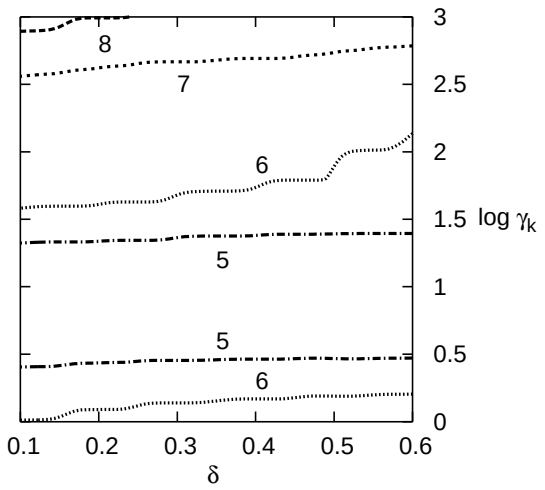

Fig. 5. Contour plot of ϵ_k for $\gamma_R = 1e^5$ and $\gamma_\eta = 1e^3$ in function of γ_k and δ.

In fact, the L_1 error norm only gives a rough indication on the performance of the algorithm. In particular, results of same L_1 error norm may correspond to images with quite different aspects. This is illustrated in Figure 6. The three images were obtained with $\gamma_R = 1e^5$, $\gamma_\eta = 1e^3$ and $\gamma_k = 1e^1$. From left to right, the value of δ was 0.1, 0.3 and 0.6, respectively. The resulting L_1 error norm was then 4.7, 4.4 and 4.7. As expected, the image obtained with the smallest value of δ seems less noisy, and it exhibits more homogeneous regions, while the image obtained with the largest value of δ seems more noisy. The issue of defining the most appropriate error measure is obviously application dependent, and it is not in the scope of this article. Anyway, the L_1 error norm remains useful as a rough indicator of the algorithm performance. On the other hand, we can rely on reproducibility to address the question of hyperparameter selection: as long as objects with similar structures are observed using similar acquisition parameters, the same hyperparameter values will tend to produce equally good (or bad) results. Therefore, in the following tests, the hyperparameters have been maintained constant at the values given by (10).

5.1.2. *Comparison of the results for different configurations*

Table 2 makes a comparison of performance between the proposed method, the unregularized version (*i.e.,* $\gamma_R = \gamma_\eta = \gamma_k = 0$), the version without the estimation of the non-multiplicative bias field (*i.e.,* step (ii) is skipped), and the direct method.

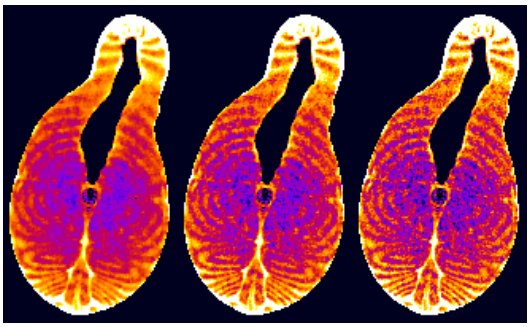

Fig. 6. (k_{1l}) estimated with $\gamma_R = 1e^5$, $\gamma_\eta = 1e^3$ and $\gamma_k = 1e^1$. From left to right: $\delta = 0.1$, 0.3 and 0.6. The corresponding L_1 error norm is 4.7, 4.4 and 4.7.

	Relative L_1 error norm
Complete method	4.4%
Unregularized version	7.4%
Without estimation of η	6.6%
Direct method	7.4%

Table 2
L_1 error norm for different configurations.

A proper choice of hyperparameter values provided a minimum value of L_1 error norm of 4.4%.

Without any regularization, the error raised up to 7.4%. That is, regularization provides a gain of 3%. In the context of food-product applications, such a gain is far from negligible. A variation of 1% in a tissue proportion inside the product is relevant, for instance to study the genotype effect on the growth of fish.

In the case where the non-multiplicative bias field is not estimated, the error was 6.6%. This points out the interest to take account of the non-multiplicative part of the model in real situations comparable to the simulated one.

Finally, the direct method produced an error of 7.4%, as the unregularized version of the proposed method. This is not surprising since the general goal of the latter is to minimize the first term of $\mathcal{J}$, while the former cancels it in the studied case (up to the approximation $E_1 \approx 0$).

5.2. *Image results*

5.2.1. *Correction results on noisy images*

The two left-hand images of Figure 7 are two of the five images acquired on the same slice of the

trout, at different positions in the MR system, in the high noise situation. The two corresponding corrected images are at right-hand side.

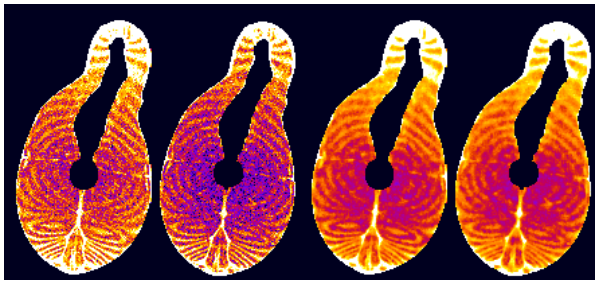

Fig. 7. From left to right: Original images acquired from at 0 mm and 45 mm from the centre of the MR system, and corresponding corrected images.

The effects of the RF inhomogeneities are clearly visible on the original images. In particular, the image at 45 mm is of lower amplitude. After correction, the two images exhibit a similar range of grey levels. Moreover, the level of the noise is lower in the corrected images while the existing structure keeps visible thanks to the edge preserving restoration. Histograms of signal intensity are presented in Figure 8 for the five raw images, and in Figure 9 for the five corrected images. The histograms of the raw images significantly differ one from each other due to the inhomogeneities, while they are very much alike for the corrected images. As expected, each image exhibits a narrower histogram once corrected.

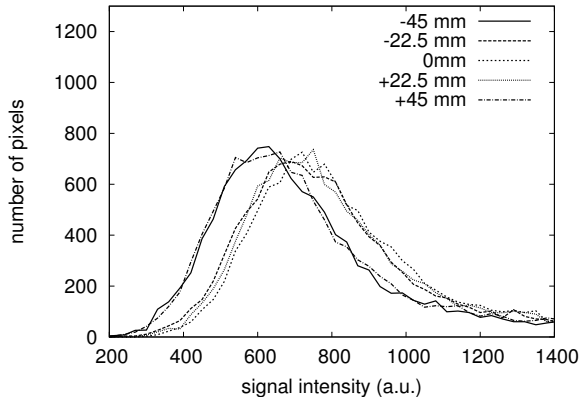

Fig. 8. Histograms of signal intensity for the five original images.

Figure 10 shows the histograms of grey levels of the five images after only partial correction: only $\boldsymbol{R}$ was estimated and compensated for, while $\boldsymbol{\eta}$ was assumed equal to one. This configuration is equivalent

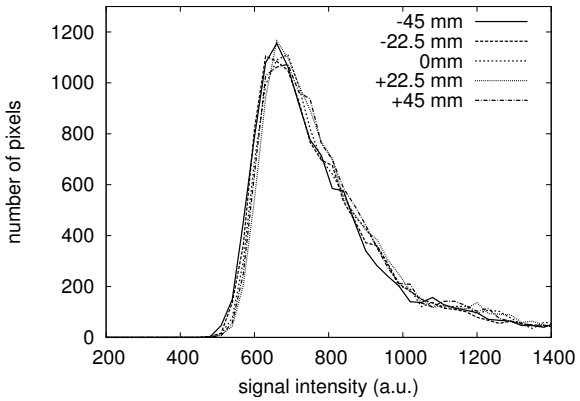

Fig. 9. Histograms of signal intensity for the five corrected images.

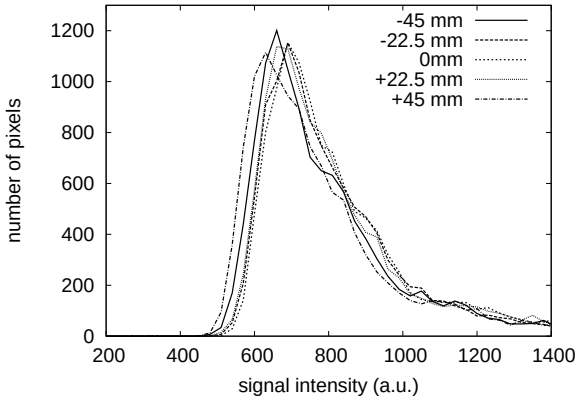

Fig. 10. Histograms of the five noisy images corrected without the estimation of η.

to the modeling of the inhomogeneities by a multiplicative bias field. The result shows that it is not sufficient to estimate the multiplicative bias $\boldsymbol{R}$ only. This is especially true in the areas that contain more muscle, since TR/T_1 is lower in such areas, and thus the non-multiplicative bias is higher.

5.2.2. *Effect of regularization*

In order to quantify the effect of regularization, the results obtained with high-noise images were compared to the results obtained in the low-noise case. Figure 11 shows the L_1 norm of the difference between $\boldsymbol{k}_1$ estimated in the high-noise case (with and without regularization) and in the low-noise case (without regularization). Since proportions estimated from low-noise images have been used instead of the unknown, true proportions, the values of the gains should be considered as relative rather than absolute. Depending on the position, the gain is

between 2.8 and 3.2% thanks to regularization. This represents a significant and homogeneous improvement, which confirms the simulated study, where a gain of 3% was obtained using the regularization scheme.

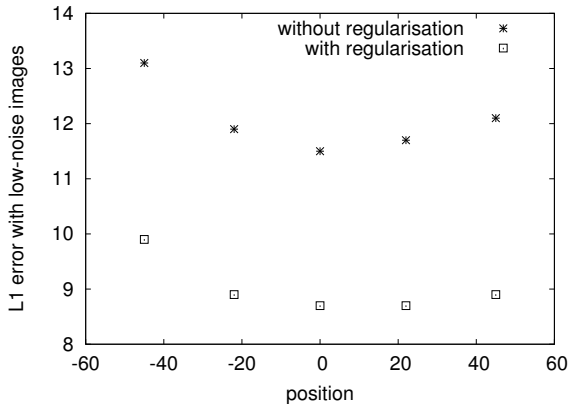

Fig. 11. L_1 error norm, between $\boldsymbol{k}_1$ obtained with high-noise images (with and without regularization) and $\boldsymbol{k}_1$ obtained with low-noise images (without regularization).

6. Conclusion

We have proposed a correction method for inhomogeneities of RF pulses and RF reception in MRI systems. It is based on a model of the measured signal as a sum of contributions of different tissues, which accounts for the fact that different tissues yield different responses regarding the RF pulse values, particularly in the case of $\boldsymbol{T_1}$-weighted images.

Here, we did not make the assumption of piecewise constant regions in the image. Actually, the latter assumption can be considered as valid in the foremost application of cerebral imaging, but it is oversimplifying in other contexts, such as food-product applications. Therefore, our approach is rather based on the processing of several images, acquired at different measurement parameter values.

A penalized least-squares criterion was defined to balance a data fidelity term and regularization terms for the RF pulses and reception maps. A non-quadratic regularization was applied to the image content, in order to reduce the noise while preserving the edges. The resulting method proved to be efficient on a fish slice with a two-tissue model, using a set of three images, two of which being acquired on an oil phantom.

Simulation results showed that our method decreases the L_1 error norm from 7.4 to 4.4% on the estimation of the tissue proportion, compared to a classical method based on a direct computation. These results showed that regularization improves the performance of the method and that the estimation of the non-multiplicative bias field has a significant impact. We have also shown that the choice of the hyperparameters is not critical. Finally, results on real images acquired on a fish confirmed the simulation results.

In order to improve the method and to enlarge the potential applications, several points remain to be explored. First, the acquisition time is a key point in MRI. Our method needs at least $I + 1$ images, with I the number of existing tissues. One possibility is to use images acquired on phantoms once and for all, which does not penalize the acquisition time. However, inhomogeneities due to patient-specific geometrical and electrical properties are not accounted for by phantom images. Fortunately, the mismatch between objects and phantoms is limited in low-field imaging. However, it remains a source of systematic error that would disappear if all images were acquired on the object. Then, shorter acquisition times should be used. This can be done with shorter TR or with fast spin-echo sequences to get additional, less accurate images, but in lesser time. As our approach is regularized, we can hope that a certain level of degradation in the data will not affect the quality of the results.

Another keypoint of the method is the required knowledge of several constants. In particular, we are currently studying the possibility to estimate the constant references O^i jointly with the other unknown quantities.

References

Belaroussi, B., Milles, J., Carme, S., Zhu, Y. M., Benoit-Cattin, H., 2006. Intensity non-uniformity correction in MRI: Existing methods and their validation. Med. Image. Anal. 10 (2), 234–246.

Bezdek, J., Hathaway, R., Howard, R., Wilson, C., Windham, M., 1987. Local convergence analysis of a grouped variable version of coordinate descent. J. Optim. Theory Appl. 54 (3), 471–477.

Blümich, B., 2000. NMR imaging of materials. Monographs on the physics and chemistry of materials. Oxford Univesity Press.

Böhning, D. B., Lindsay, B. G., 1988. Monotonicity of quadratic-approximation algorithms. Ann. Inst. Stat. Math. 40, 641–663.

Brinkmann, B., Manduca, A., Robb, R., 1998. Optimized homomorphic unsharp masking for MR grayscale inhomogeneity correction. IEEE Trans. Medical Imaging 17 (2), 161–171.

Collewet, G., Davenel, A., Toussaint, C., Akoka, S., 2002. Correction of intensity nonuniformity in spin-echo T1-weighted images. Magn. Reson. Imaging 20 (4), 365–373.

Condon, B., Patterson, J., Wyper, D., Jenkins, A., Hadley, D., 1987. Image non-uniformity in magnetic resonance imaging : its magnitude and methods for its correction. Brit. J. Radiol. 60 (709), 83–87.

Daanen, V., Coste, E., Sergent, G., Godart, F., Vasseur, C., Rousseau, J., 2000. Accurate localization of needle entry point in interventional MRI. J. Magn. Reson. Imaging 12 (4), 645–649.

Fan, A., Wells III, W., Fisher III, J., Müjdat, Ç., Haker, S., Mulkern, R., Tempany, C., Willsky, A., 2003. A unified variational approach to denoising and bias correction in MR. In: Information Proc Med Imaging. pp. 148–159.

Grenier, A., Lucas, T., Collewet, G., Le Bail, A., 2003. Assessment by MRI of local porosity in dough during proving. Theoretical considerations and experimental validation using a spin-echo sequence. Magn. Reson. Imaging 21 (9), 1071–1086.

Guillemaud, R., Brady, M., 1997. Estimating the bias field of MR images. IEEE Trans. Medical Imaging 16 (3), 238–251.

Haacke, E., Brown, R., Thompson, M., Venkatesan, R., 1999. Magnetic Resonance Imaging: Physical Principles and Sequence Design. Wiley-Liss.

Hills, B., 1998. Magnetic resonance imaging in food science. Wiley-Interscience.

Hou, Z., 2006. A review on MR image intensity inhomogeneity correction. Int. J. Biomed. Imaging 2006, 1–11.

Koivula, A., Alakuijala, J., Tervonen, O., 1997. Image feature based automatic correction of low-frequency spatial intensity variations in MR images. Magn. Reson. Imaging 15 (10), 1167–1175.

Labat, C., Idier, J., 2007. Convergence of conjugate gradient methods with a closed-form stepsize formula. J. Optim. Theory Appl. 135 (2).

Lange, K., Hunter, D., Yang, I., 2000. Optimization transfert unsing surrogate objective functions. J. Comput. Graph. Statist. 9 (1), 1–20.

Luenberger, D. G., 1997. Optimization by Vector Space Methods. John Wiley & Sons, Inc., New York, NY, USA.

Marden, F. A., Connolly, A. M., Siegel, M. J., Rubin, D. A., 2005. Compositional analysis of muscle in boys with duchenne muscular dystrophy using MR imaging. Skeletal Radiology 34 (3), 140–148.

McVeigh, E., Bronskill, M., Henkelman, R., 1986. Phase and sensitivity of receiver coils in magnetic resonance imaging. Med. Phys. 13 (6), 806–814.

Merl, T., Scholz, M., Gerhardt, P., Langer, M., Laubenberger, J., Weiss, H. D., Gehl, H. B., Wolf, K. J., Ohnesorge, I., 1999. Results of a prospective multicenter study for evaluation of the diagnostic duality of an open whole-body low-field MRI unit. A comparison with high-field MRI measured by the applicable gold standard. Eur. J. Radiol. 30 (1), 43–53.

Nowak, R. D., 1999. Wavelet-based Rician noise removal for magnetic resonance imaging. IEEE Trans. Medical Imaging 8 (10), 1408–1419.

Press, W. H., Flannery, B. P., Teukolsky, S. A., Vetterling, W. T., 1988. Numerical Recipes: The Art of Scientific Computing. Cambridge University Press.

Prima, S., Ayache, N., Barrick, T., Roberts, N., 2001. Maximum likelihood estimation of the bias field in MR brain images : Investigating different modelings of the imaging process. In: MICCAI. Springer-Verlag Berlin Heidelberg, pp. 818–819.

Robb, D., Kestin, S., Warriss, P., Nute, G., 2002. Muscle lipid content determines the eating quality of smoked and cooked atlantic salmon (salmo solar). Aquaculture 205 (3-4), 345–358.

Sequeiros, R. B., Reinikainen, H., Sequeiros, A. M. B., Vaara, T., Ojala, R., Paakko, E., Tervonen, O., 2007. MR-guided breast biopsy and hook wire marking using a low-field (0.23 T) scanner with optical instrument tracking. European Radiology 17 (3), 813–819.

Sijbers, J., Den Dekker, A., Van Audekerke, J., Verhoye, M., Van Dick, D., 1998. Estimation of the noise in magnitude MR images. Magn. Reson. Imaging 16 (1), 87–90.

Sled, J. G., Pike, G. B., 1998. Standing-wave and RF penetration artifacts caused by elliptic geometry: An electrodynamic analysis of MRI. IEEE Trans. Medical Imaging 17 (4), 653–662.

Sled, J. G., Pike, G. B., 2000. Correction for B_1 and B_0 variations in quantitative T_2 measurements using MRI. Magn. Reson. Med. 43 (4), 589–593.

Sled, J. G., Zijdenbos, A. P., Evans, A. C., 1998. A nonparametric method for automatic correction of intensity nonuniformity in MRI data. IEEE Trans. Medical Imaging 17 (1), 87–97.

Tincher, M., Meyer, C. R., Gupta, R., Williams,

D. M., 1993. Polynomial modeling and reduction of RF body coil spatial inhomogeneity in MRI. IEEE Trans. Medical Imaging 12 (2), 361–365.

Tofts, P. S., Barker, G. J., Simmons, A., Macmanus, D. G., Thorpe, J., Gass, A., Miller, D. H., 1994. Correction of nonuniformity in images of the spine and optic- nerve from fixed receive-only surface coils at 1.5-T. J. Comput. Assist. Tomogr. 18 (6), 997–1003.

Toussaint, C., Fauconneau, B., Medale, F., Collewet, G., Akoka, S., Haffray, P., Davenel, A., 2005. Description of the heterogeneity of lipid distribution in the flesh of brown trout (salmo trutta) by MR imaging. Aquaculture 243 (1-4), 255–267.

Van Leemput, K., Maes, F., Vandermeulen, D., Suetens, P., 1999. Automated model-based bias field correction of MR images of the brain. IEEE Trans. Medical Imaging 18 (10), 885–896.

Vovk, U., Pernus, F., Likar, B., 2007. A review of methods for correction of intensity inhomogeneity in mri. IEEE Trans. Medical Imaging 26 (3), 405–421.

Wang, J., Qiu, M., Constable, R., 2005. In vivo method for correcting transmit/receive nonuniformities with phased array coils. Magn. Reson. Med. 53 (3), 666–674.

Wells, W., Kikinis, R., Grimson, W., Jolesz, F., 1996. Adaptive segmentation of MRI data. IEEE Trans. Medical Imaging 15 (4), 429–422.

Zhang, Y., Brady, M., Smith, S., 2001. Segmentation of brain MR images through a hidden Markov random field model and the expectation-maximization algorithm. IEEE Trans. Medical Imaging 20 (1), 45–57.

7. Appendix: the Hessian of $\mathcal{J}$ w.r.t. $\boldsymbol{\eta}$ is upper bounded

The object of the present appendix is to show that the criterion $\mathcal{J}$ defined by (5) has an upper bounded Hessian $\nabla^2\mathcal{J}(\boldsymbol{\eta}) = (\partial^2\mathcal{J}/\partial\eta_k\partial\eta_\ell)$, *i.e.,* that there exists a constant, symmetric, positive definite matrix $\mathbf{M}$ such that $\mathbf{M} - \nabla^2\mathcal{J}(\boldsymbol{\eta})$ is positive semidefinite for any $\boldsymbol{\eta}$. This mathematical condition is a prerequisite to ensure the convergence of easily implemented algorithms, either of the quasi-Newton type (Lange et al., 2000), or of the CG type (Labat and Idier, 2007).

As a function of $\boldsymbol{\eta}$, the objective function $\mathcal{J}$ defined by (5) takes the following form:

$$\mathcal{J}(\boldsymbol{\eta}) = \sum_{\ell=1}^{L} \mathcal{J}_\ell(\eta_\ell) + \gamma_\eta \left\|\mathbf{D}\boldsymbol{\eta}\right\|^2 + c_\eta \qquad (11)$$

where c_η does not depend on $\boldsymbol{\eta}$, and

$$\mathcal{J}_\ell(\eta) = \sum_{j=1}^{J} \lambda_j \left(s_{j\ell} - \sum_{i=1}^{I} C_{ij\ell} f(\eta, \theta_j, T_{1i}) \right)^2 \qquad (12)$$

with $C_{ij\ell} = R_\ell O_{ji} k_{\ell i}$. From (11), it is easy to express the Hessian of $\mathcal{J}$ w.r.t. $\boldsymbol{\eta}$ under the following form:

$$\nabla^2\mathcal{J}(\boldsymbol{\eta}) = \operatorname{diag}\left(\frac{\partial^2\mathcal{J}_\ell}{\partial\eta_\ell^2}\right) + 2\gamma_\eta \mathbf{D}^{\mathrm{t}}\mathbf{D}. \qquad (13)$$

Let $F_{ij}^d(\eta) = \partial^d f(\eta, \theta_j, T_{1i})/\partial\eta^d$. According to (12), the second derivative of $\mathcal{J}_\ell$ is given by:

$$\frac{\partial^2\mathcal{J}_\ell}{\partial\eta^2} = \sum_{j=1}^{J} \lambda_j \left(\sum_{i,k=1}^{I} C_{ij\ell} C_{kj\ell} M_{ikj}(\eta)) - 2 s_{j\ell} \sum_{i=1}^{I} C_{ij\ell} N_{ij}(\eta) \right)$$

where $N_{ij}(\eta) = F_{ij}^2(\eta)$ and

$$M_{ikj}(\eta) = 2F_{ij}^1(\eta)F_{kj}^1(\eta) + F_{ij}^2(\eta)F_{kj}^0(\eta) + F_{ij}^0(\eta)F_{kj}^2(\eta)$$

Now, let us denote $f^{\max} = \max_\eta f(\eta)$ and $f^{\min} = \min_\eta f(\eta)$ for any function f that depends on η. Then,

$$\frac{\partial^2\mathcal{J}_\ell}{\partial\eta^2} \leqslant b_\ell \qquad (14)$$

with

$$b_\ell = \sum_{j=1}^{J} \lambda_j \left(\sum_{i,k=1}^{I} C_{ij\ell} C_{kj\ell} \mu_{ikj\ell} - 2 s_{j\ell} \sum_{i=1}^{I} C_{ij\ell} \nu_{ij\ell} \right)$$

and

$$\mu_{ikj\ell} = \begin{cases} M_{ikj}^{\max} & \text{if } C_{ij\ell}C_{kj\ell} > 0 \\ M_{ikj}^{\min} & \text{otherwise} \end{cases}$$

$$\nu_{ij\ell} = \begin{cases} N_{ij}^{\max} & \text{if } C_{ij\ell} < 0 \\ N_{ij}^{\min} & \text{otherwise} \end{cases}$$

Finally, let

$$\mathbf{M} = \operatorname{diag}(b_\ell) + 2\gamma_\eta \mathbf{D}^{\mathrm{t}}\mathbf{D}. \qquad (15)$$

From (13) and (14), it is obvious that $\mathbf{M} - \nabla^2\mathcal{J}(\boldsymbol{\eta})$ is a positive semidefinite matrix.

In practice, the quantities $M_{ikj}^{\max}$, $M_{ikj}^{\min}$, $N_{ij}^{\max}$ and $N_{ij}^{\min}$ can be approximately computed and stored once for all, using a fine discretization of η between a lower and an upper bound. Finally, let us remark that the quantities $C_{ij\ell} = R_\ell O_{ji} k_{\ell i}$ are

expected to be positive, so that the computation of $M_{ikj}^{\min}$ and $N_{ij}^{\max}$ should be useless. However, we have chosen not to enforce the inequality constraints $R_\ell > 0$ and $k_{\ell i} \in [0, 1]$ in the minimization process, for the sake of simplicity. Therefore, $C_{ij\ell} > 0$ is most often true, but not always.